Physical models of the bidirectional reflectance of solar receiver coatings

Moritz Bitterling*, Gregor Bern, Helen Rose Wilson, Anna Heimsath, Peter Nitz

Fraunhofer Institute for Solar Energy Systems ISE, Heidenhofstr. 2, 79110 Freiburg, Germany

Abstract

We present measurements of the Bidirectional Reflectance Distribution Function (BRDF) of the state-of-the art solar receiver coating, Pyromark® 2500, and show how the data can be accurately described with physical models. In the conducted measurements of the receiver coating, a peak shift of the radiation away from the direction of ideal specular reflection was observed. Both the Cook–Torrance and the He–Torrance models reproduce this behaviour. For the application of the former model, an empirical angular dependence of the parameter describing the surface roughness has to be assumed in order to obtain an adequate fit to the data. The latter model is less exact in a statistical sense, but it is physically based, with six meaningful fit parameters. As we found that the He–Torrance model with its original form of the specular reflection yielded physically incorrect results for incidence angles larger than 80°, a modification is proposed to overcome this deficiency.

Overall, the fitted models are able to provide a good description of the BRDF of the receiver coating over three orders of magnitude. Our results can play an important role in facilitating camera-based flux control or optical simulations of solar tower systems. Moreover, we think that our findings can serve as a sound starting point for the physical modelling of other absorber coatings currently being developed.

Keywords: Central receiver solar tower systems, Solar absorbers, Coating, Optical properties, Reflectance, Cook–Torrance model, He–Torrance model, BRDF

1. Introduction

Central Receiver Systems (CRS) transform the incident concentrated solar flux into usable high temperature heat for electricity generation or high-temperature processes. The interface between the solar flux and the thermodynamic cycle is the central receiver, located at the top of a tower in the centre of the solar field, thousands of sun-tracking heliostats, that reflect the direct solar flux to the receiver. In commercial CRS, the receiver is composed of coated tube bundles, through which the heat transfer medium flows, that transports the absorbed energy to the subsequent process. The coating must resist a temperature of more than 600 °C, up to 1000 °C, while at the same time featuring high absorptance in the solar spectrum and preferably low emittance in the infra-red range.

The state-of-the-art receiver coating fpr CRS is the high-temperature paint Pyromark 2500 (Ambrosini et al., 2019), manufactured by *Tempil*. Different studies have been conducted on the optical performance of the paint with respect to the thickness of application and the substrate (Coventry and Burge, 2017) or curing temperatures and durability under high temperatures, e.g. by Ho et al. (2012). Furthermore, this absorber coating is used as a reference standard for the development of new coatings or structured surfaces for concentrating solar power (CSP),

*Corresponding author

Email address: moritz.bitterling@ise.fraunhofer.de (Moritz Bitterling)

Nomenclature

Abbreviations

BRDF	bidirectional reflectance distribution function
CRS	Central Receiver System
CSP	Concentrating Solar Power
CT	Cook–Torrance (model)
HT	He–Torrance (model)

Subscripts

i	incident radiation
Lam	Lambertian
m	microfacet
r	reflected radiation

Symbols

A	illuminated surface (m^2)
c_{pg}	proportionality constant of photogoniometer ($W \cdot sr^{-1} \cdot A^{-1}$)
D	microfacet distribution in CT model (sr^{-1})
E_i	irradiance ($W \cdot m^{-2}$)
F	Fresnel reflectance (–)
f_r	bidir. refl. distribution function (sr^{-1})
G	shadowing factor (–)
$\mathbf{i}$	incidence unit vector
I	radiant intensity ($W \cdot sr^{-1}$)
L	radiance ($W \cdot m^{-2} \cdot sr^{-1}$)
n	index of refraction (–)
$\mathbf{r}$	reflection unit vector
R_{dh}	directional hemispherical reflectance factor (–)
S_r	signal from a sample, measured with the photogoniometer (A)
S_i	signal of the unobstructed beam, measured with the photogoniometer (A)
w	opening angle of specular cone
Φ	radiant flux (W)
ϕ	azimuth angle
θ	polar angle
α	roughness parameter in CT model (–)
σ	vertical roughness scale in HT model (m)
τ	horizontal roughness scale in HT model (m)
$\sqrt{\chi^2_{red}}$	regression standard error (–)
ω	solid angle (sr)
Ω_{beam}	solid angle of the unobstructed beam in the photogoniometer (sr)

as shown by Ho et al. (2012), Tsuda et al. (2018) or Rubin et al. (2019).

The description of the receiver coating using the BRDF allows for the derivation of the directional absorptance and the evaluation of secondary reflections within an optimized receiver geometry (e.g. cavities) or the analysis of

glare and its impact on the environment of a CRS. Measurement procedures analyzing the reflected flux from the receiver, such as flux density distribution measurements (e.g. described by Röger et al. (2014)) or heliostat *in situ* calibration or closed-loop tracking strategies as described by Bern et al. (2019), may use the BRDF for the correction of the primary camera input signals taken from the receiver. Measurements of samples in the laboratory as described in this paper or *in situ* measurements (e.g. Offergeld et al., 2019) can provide a useful database for such applications. Especially *in situ* measurements can be very challenging, when a high angular resolution is required. Models describing the BRDF at a semi-empirical level allow the approximation of a complete data set with reduced measurement effort. By fitting the model parameters to the measured data points, accurate values can be obtained if the model shows good agreement with the actual shape of the distribution.

In this paper, we present a selection of models to reproduce the BRDF of surfaces fitted to 3-dimensional measurement data. Two models from literature and one adapted model are analyzed for their suitability to describe the sample. As an example for receiver coatings we use a sample of Pyromark 2500 measured in a 3-dimensional scanning photogoniometer.

In the following section, the BRDF is introduced as a theoretical framework to describe the angle-dependent reflectance of a surface, and two different established BRDF models are shown. In Section 3, the experimental procedure for obtaining a BRDF is described and the two models are used to describe the measured data. Subsequently, possible adaptions of the model are shown which lead to a better fit with the data (Section 4). The conclusion on the achieved results is given in Section 6.

2. Theoretical background

2.1. Definition of the BRDF

The *bidirectional reflectance distribution function* f_r of a uniform and plane surface is defined as the ratio of differential reflected radiance $\mathrm{d}L_\mathrm{r}$ and differential irradiance $\mathrm{d}E_\mathrm{i}$ (Nicodemus et al., 1977; Stover, 1995; ASTM, 2005):[1]

$$f_\mathrm{r} = \frac{\mathrm{d}L_\mathrm{r}}{\mathrm{d}E_\mathrm{i}} \tag{1}$$

Geometrical definitions of f_r are shown in Fig. 1, with $\mathbf{i}$ and $\mathbf{r}$ denoting the directions of incident and reflected radiation.

The reflected radiance is the radiant flux $\mathrm{d}\Phi_\mathrm{r}$ per solid angle $\mathrm{d}\omega_\mathrm{r}$ and projected area $\mathrm{d}A{\cdot}\cos\theta_\mathrm{r}$, and the irradiance is the incident radiant flux $\mathrm{d}\Phi_\mathrm{i}$ per area $\mathrm{d}A$:

$$L_\mathrm{r}(\mathbf{i},\mathbf{r}) = \frac{\mathrm{d}\Phi_\mathrm{r}(\mathbf{i},\mathbf{r})}{\mathrm{d}\omega_\mathrm{r}\cdot\mathrm{d}A\cdot\cos\theta_\mathrm{r}} \tag{2}$$

$$E_\mathrm{i}(\mathbf{i}) = \frac{\mathrm{d}\Phi_\mathrm{i}(\mathbf{i})}{\mathrm{d}A} \tag{3}$$

If the total illuminated area A is very small, as in a photogoniometer, the surface element $\mathrm{d}A$ in Eq. 2 can be replaced by A and $\mathrm{d}\Phi_\mathrm{i}$ by Φ_i, which is the total radiant flux received by A. This yields with Eq. 1

$$f_\mathrm{r}(\mathbf{i},\mathbf{r}) = \frac{\mathrm{d}\Phi_\mathrm{r}(\mathbf{i},\mathbf{r})}{\mathrm{d}\omega_\mathrm{r}\cdot\cos\theta_\mathrm{r}\cdot\Phi_\mathrm{i}}\ , \tag{4}$$

which is an expression that can be used to calculate the BRDF from data measured with a photogoniometer.

If a sample is characterized in a photogoniometer, the measured signal S_r is proportional to the reflected radiant intensity I_r with a proportionality factor c_pg:

$$c_\mathrm{pg}\cdot S_\mathrm{r}(\mathbf{i},\mathbf{r}) = I_\mathrm{r}(\mathbf{i},\mathbf{r}) = \frac{\mathrm{d}\Phi_\mathrm{r}(\mathbf{i},\mathbf{r})}{\mathrm{d}\omega_\mathrm{r}} \tag{5}$$

The incident radiant flux Φ_i can be determined by integrating the radiant intensity or rather the measurement

[1] In this article, the physics nomenclature used by Stover (1995) is adopted, in contrast to the one that is common among the engineering community (see Modest (2003) or Siegel and Howell (1992)).

signal S_i of the unobstructed beam, which is done during a reference measurement without a sample (Apian-Bennewitz, 2010):

$$\Phi_\mathrm{i} = \int_{\Omega_\mathrm{beam}} I_\mathrm{i}(\mathbf{i}) \cdot \mathrm{d}\omega_\mathrm{i} = \int_{\Omega_\mathrm{beam}} c_\mathrm{pg} \cdot S_\mathrm{i}(\mathbf{i}) \cdot \mathrm{d}\omega_\mathrm{i} \quad (6)$$

Inserting Eqs. 5 and 6 into Eq. 4 allows the calculation of the BRDF from measured data, without requiring knowledge of c_pg:

$$f_\mathrm{r}(\mathbf{i},\mathbf{r}) = \frac{S_\mathrm{r}(\mathbf{i},\mathbf{r})}{\cos\theta_\mathrm{r} \cdot \int_{\Omega_\mathrm{beam}} S_\mathrm{i}(\mathbf{i}) \cdot \mathrm{d}\omega_\mathrm{i}} \quad (7)$$

2.2. Directional hemispherical reflectance factor

From a known BRDF, the *directional hemispherical reflectance factor* R_dh can be calculated by integrating the function over the whole hemisphere (Eq. 8). An additional factor $\cos(\theta_\mathrm{r})$ in the integrand arises from the projection of the surface onto the hemisphere:

$$R_\mathrm{dh}(\mathbf{i}) = \int_0^{2\pi} \int_0^{\pi/2} \cos(\theta_\mathrm{r}) \cdot f_\mathrm{r}(\mathbf{i},\mathbf{r}) \cdot \sin(\theta_\mathrm{r}) \cdot \mathrm{d}\theta_\mathrm{r}\mathrm{d}\phi_\mathrm{r} \quad (8)$$

For a perfect Lambertian reflector, which is characterized by a constant BRDF $f_\mathrm{r,Lam}$ that is independent of incidence and reflection angles, Eq. 8 yields the following relation between BRDF and reflectance factor $R_\mathrm{dh,Lam}$:

$$f_\mathrm{r,Lam} = \frac{R_\mathrm{dh,Lam}}{\pi} \quad (9)$$

Cook–Torrance (CT) microfacet model

Microfacet models were introduced by Torrance and Sparrow (1967) and further refined by Cook and Torrance (1982), who included findings of Beckmann and Spizzichino (1963) concerning the statistics of rough surfaces. The models describe a surface as a collection of statistically distributed, small and planar facets. For given incidence and reflection angles[2], reflection takes place on all microfacets with the surface normal characterized by the polar angle

$$\theta_\mathrm{m} = \frac{\theta_\mathrm{i} + \theta_\mathrm{r}}{2} \,. \quad (10)$$

Shadowing and masking between the facets towards grazing incidence is taken into account by microfacet models, but due to the geometrical nature of the models, wave-optical effects are neglected. The Cook–Torrance microfacet BRDF has the following form[2]:

$$f_\mathrm{r,CT} = \frac{D(\theta_\mathrm{m},\alpha) \cdot F(\frac{\theta_\mathrm{i}-\theta_\mathrm{r}}{2}, n) \cdot G(\theta_\mathrm{i},\theta_\mathrm{r},\alpha)}{4 \cdot \cos\theta_\mathrm{i} \cdot \cos\theta_\mathrm{r}} + \frac{R_\mathrm{dh,Lam}}{\pi} \quad (11)$$

D is the microfacet distribution, describing the fraction of facets with polar angles θ_m, which depends on one roughness parameter α. F is the Fresnel reflectance for specular reflection from a smooth surface with index of refraction[3] n. G is a factor taking shadowing and masking effects into account. The second summand describes an angle-independent part of the radiation which is scattered uniformly diffusely as for a Lambertian reflector (see Eq. 9),

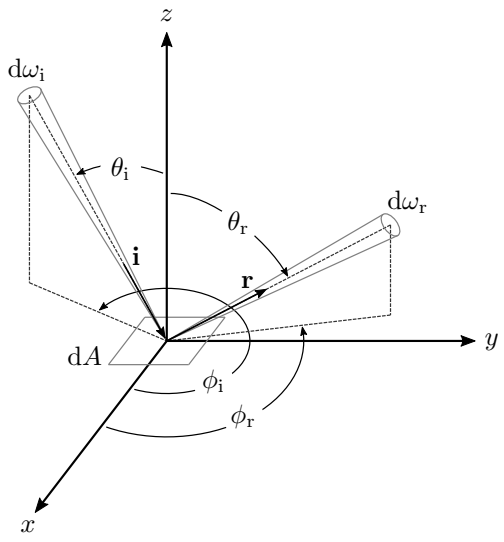

Figure 1: Geometrical definitions of incident and reflected radiation on a small surface element dA (adapted from Nicodemus et al. (1977)). For convenience, the polar angle θ_r is allowed to take negative values, implying a 180° rotation: $(-\theta_\mathrm{r}, \phi_\mathrm{r}) := (\theta_\mathrm{r}, \phi_\mathrm{r} + \pi)$.

[2]For the sake of clarity, the equations are only given for reflection in the plane of incidence, implying a constant ϕ_r and $\theta_\mathrm{r} \in [-\pi/2, \pi/2]$. A derivation of the vectorial expression for arbitrary ϕ_r is given by Walter et al. (2007).

[3]Throughout this work, the index of refraction is assumed to be a real number. Omitting its imaginary part and using a real approximation does not change the angular dependence of the Fresnel coefficient considerably, if the imaginary part is small. We assume that this is the case for Pyromark.

which is an approximation for multiple surface scattering events and volume scattering.

The expression for F is well-known and therefore not given here, but there is some flexibility in choosing D and G, depending on the assumptions concerning surface statistics. In the original Cook–Torrance model, the microfacet normals are assumed to follow the Beckmann distribution, which is derived from the Gauss distribution. However, following a suggestion of Walter et al. (2007), we found that the GGX/Trowbridge–Reitz distribution (Trowbridge and Reitz, 1975) is better suited to model our data, since it gives more weight to steep facets than the Beckmann distribution. The term D for the distribution of the microfacet polar angle θ_m has the following form if the GGX distribution is used:

$$D_\mathrm{ggx}(\theta_\mathrm{m}, \alpha) = \frac{\alpha^2}{\pi\,(\alpha^2\,\cos^2\theta_\mathrm{m} + \sin^2\theta_\mathrm{m})^2} \qquad (12)$$

The roughness parameter α controls the width of the distribution. It is connected with the mean slope m_CT of all microfacets, which can be found by evaluating $\langle\tan\theta_\mathrm{m}\rangle$ over the hemisphere for the distribution of Eq. 12:

$$m_\mathrm{CT} = \langle\tan\theta_\mathrm{m}\rangle = \alpha\cdot\pi/2\ . \qquad (13)$$

A suitable shadowing factor is the Smith shadowing factor G_S (Smith, 1967), which is also derived by Walter et al. (2007) for this distribution:

$$G_\mathrm{S}(\theta_\mathrm{i}, \theta_\mathrm{r}, \alpha) = G_{S1}(\theta_\mathrm{i}, \alpha)\cdot G_{S1}(\theta_\mathrm{r}, \alpha) \qquad (14)$$

$$G_{S1}(\theta, \alpha) = \frac{2}{1+\sqrt{1+\alpha^2\,\tan^2\theta}} \qquad (15)$$

A major advantage of the Cook–Torrance model is that it is relatively simple and gives absolute values of the BRDF, depending only on three (fit) parameters n, α and $R_\mathrm{dh,Lam}$.

He–Torrance wave-optical model

The He–Torrance (HT) model (He et al., 1991) extends the Cook–Torrance model to the physical optics region and includes a smooth transition from diffuse to specular reflection as the surface roughness is decreased or grazing incidence is approached. It is derived by solving the Kirchhoff integral of scalar diffraction theory, taking shadowing effects into consideration. Surfaces are described in a statistical manner, with a Gaussian height distribution and a horizontal autocorrelation length.

Just as in the Cook–Torrance model, the BRDF in the He–Torrance model $f_\mathrm{r,HT}$ also has a uniform ideal diffuse component $f_\mathrm{r,Lam}$. The directional share consists of the directional diffuse part $f_\mathrm{r,dd}$ and the specular part $f_\mathrm{r,sp}$:

$$f_\mathrm{r,HT} = f_\mathrm{r,sp} + f_\mathrm{r,dd} + f_\mathrm{r,Lam} \qquad (16)$$

The two directional components contain the Fresnel equations with the index of refraction n as well as a vertical measure of roughness σ and a horizontal length measure τ. With $R_\mathrm{dh,Lam}$, this makes the He–Torrance model a model with four (fit) parameters. For the rather complex expression of $f_\mathrm{r,dd}$, the reader is referred to the original paper of He et al. (1991) as well as later publications (Li and Torrance, 2005a,b) which contain corrections and clarifications.

The expression for the specular term is

$$f_\mathrm{r,sp} = \frac{F(\frac{\theta_\mathrm{i}-\theta_\mathrm{r}}{2}, n)\cdot \mathrm{e}^{-g}\cdot G_\mathrm{HT}(\theta_\mathrm{i}, \theta_\mathrm{r}, \sigma, \tau)}{\cos\theta_\mathrm{i}\cdot \mathrm{d}\omega_\mathrm{i}}\cdot\Delta \qquad (17)$$

$$G_\mathrm{HT}(\theta_\mathrm{i}, \theta_\mathrm{r}, \sigma, \tau) = G_\mathrm{HT1}(\theta_\mathrm{i}, \sigma, \tau)\cdot G_\mathrm{HT1}(\theta_\mathrm{r}, \sigma, \tau)\ . \qquad (18)$$

F is the Fresnel reflectance, g a complex function of incidence and reflection angles and σ and τ, G_HT is the shadowing factor (which takes values in the interval [0,1]), $\mathrm{d}\omega_\mathrm{i}$ the solid angle of the incident beam and Δ the unit function, which is 1 only in the cone of the specular reflection. The expressions for g and G_HT1 involve a transcendental equation and are also given by He et al. (1991).

3. Experimental

3.1. Sample preparation

The BRDF measurements were made on a coated aluminium sheet with an area of 20x30 cm^2. The Pyromark 2500 coating was applied to the sheet with a paint roller

and then cured at 250 °C for 2 h, according to the product data sheet.

3.2. Measurements

Measurements on the Pyromark sample were performed in a 3D scanning photogoniometer (pgII (Apian-Bennewitz, 2010), manufactured by *pab advanced technologies Ltd*). In the photogoniometer, the sample is illuminated from different incidence angles with a halogen lamp mounted behind an IR filter, while the reflected radiation is recorded over the whole hemisphere by a photodiode with a V(λ) spectral response of the sensor, i.e. corresponding to the light-adapted human eye. If the spectrum of the lamp is weighted with the spectral response, the maximum of the distribution is at 585 nm, and the FWHM (Full width at half maximum) is 138 nm. At vertical incidence, the cross section of the illuminated spot on the sample has a diameter of 25 mm. A more detailed description of the measurement setup is given by Bitterling et al. (2020).

17 measurements were performed for different incidence angles θ_i from 0° to 80°, all with the same azimuth incidence angle[4] $\phi_\mathrm{i} = 45°$ with respect to the aluminium extrusion direction. For each incidence angle, the reflected radiation was recorded with fine spatial resolution over the whole hemisphere, each time producing a data set of roughly 600 000 irreglularly distributed points. Every data set was triangulated and linearly interpolated[5] to an almost equidistant helical grid (Bauer, 2000) to ensure an equal contribution of all directions of reflected radiation to the following model fits. The grid contains 20 000 points, which produces a mean distance of about 1.0° between adjacent data points. Fig. 2 shows the measured data for one incidence angle.

Subsequently, the measured data were normalized by the integrated beam intensity and converted to BRDF values with Eq. 7.

[4] A dependence on the azimuthal angle was not observed.

[5] Interpolation was also performed for the range of angles of reflection for which the detector head blocks the incident beam.

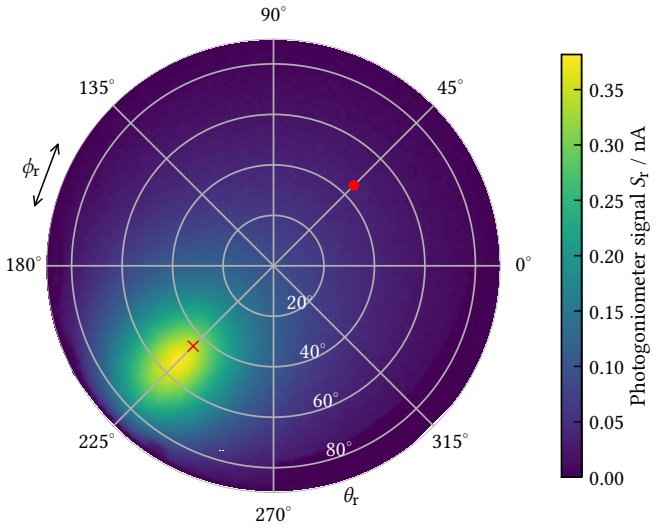

Figure 2: Measurement signal from the 3-dimensional scanning photogoniometer for Pyromark: Current caused by the reflected radiation for azimuth incidence angle ϕ_i=45° and polar incidence angle θ_i=45°. The incidence direction is marked with a dot, the angle of ideal specular reflection with a cross. A peak shift of the reflected radiation towards larger polar angles is visible.

The uncertainty on the measurement data consists of random and systematic contributions: 3 pA random error on the measurement signal and additionally 5 pA systematic uncertainty due to the zero point calibration of the current. An additional relative uncertainty of 2 % comes from the reference beam measurement and non-linearities of the components of the setup. Furthermore, there is 0.3° uncertainty on the value of the angles of reflection θ_r, which is mainly due to the extent of the illuminated spot on the sample.

3.3. Comparison of models and measured data

For the fits, measurement data up to the polar angle of reflection θ_r of 85° were used, which corresponds to 18 257 single data points per data set. The data for all 17 incidence angles θ_i were fit simultaneously with identical fit parameters, which resulted in 310 369 data points per fit.

The two different BRDF models were fit to the data using a standard least-squares minimization, where the fol-

lowing expression was minimized:

$$\sqrt{\chi^2_{\mathrm{red}}} = \sqrt{\frac{1}{\nu}\sum_j \frac{r_j^2}{\sigma_j^2}} \tag{19}$$

The residual of data point j is r_j, the uncertainty on the measurement value is σ_j and the number of degrees of freedom of the fit is ν. The value of Eq. 19 is the *standard error of the regression* and can be used as an indicator of the quality of a fit. $\sqrt{\chi^2_{\mathrm{red}}} \approx 1$ indicates an adequate fit within the measurement uncertainty, $\sqrt{\chi^2_{\mathrm{red}}} \gg 1$ signifies poor fit quality.

For all fits, the obtained fit parameters are highly correlated. This applies particularly to the pair of α and n in the Cook–Torrance model, and to the pair of σ and τ in the He–Torrance model. For this reason, no uncertainty on the best fit parameters is given. Each presented set of fit parameters should rather be seen as one possible set, but a comparable fit quality can be obtained with several sets with different parameter values.

Cook–Torrance model

Applying the CT model to our measurement data, it was not possible to obtain a fit with good quality for all incidence angles simultaneously using only the 3 fit parameters of the model. Therefore the roughness parameter α was allowed to be fit individually for each incidence angle, while the index of refraction n and the constant Lambertian part $R_{\mathrm{dh,Lam}}$ were identical for all angles. Hence all data was fitted simultaneously with a fit of 19 fit parameters, which produced the results shown in Fig. 3 for the plane of incidence (ϕ_{r}=45° or ϕ_{r}=225°). The overall standard regression error of the fit is 1.03, but there are strong local variations, which are described later. The fit results for the index of refraction and the constant Lambertian part of the reflection are

$$n_{\mathrm{CT}} = 1.43$$
$$R_{\mathrm{dh,Lam,CT}} = 0.0110\ .$$

The different values for the roughness parameter α are shown in Fig. 4.

A sigmoidal decrease of α from 0.42 to 0.24 is visible, which indicates that the surface appears smoother at high incidence angles. This behaviour has been described in the literature (He et al., 1991), but with the CT model, a physical description of the decrease can not be given. To capture the decrease quantitatively and to be able to interpolate between the values, the empirical function

$$\alpha(\theta_{\mathrm{i}}) = p_1 \cdot (1 - \tanh(p_2 \cdot (\theta_{\mathrm{i}} - p_3))) + p_4 \tag{20}$$

was fitted to the data. The obtained fit parameters are

$$p_1 = 0.1012(3) \qquad p_2 = 2.661(15)$$
$$p_3 = 51.51(5)^\circ \qquad p_4 = 0.2199(4)\ .$$

The decrease in the quality of the fit towards grazing angles as seen in Fig. 4 is attributed to the growing contribution of specular reflection, which occurs when the magnitude of the apparent surface roughness is less than the wavelength of the illuminating light. Specular behaviour of Pyromark was also observed by Ho et al. (2012) for incidence angles larger than 30°.

The regression standard error for the individual data sets rises from 0.5 at vertical incidence to almost 2 near grazing incidence. If the regression error is only evaluated in the plane of incidence, the decrease in fit quality is even more pronounced, due to the exclusion of many 'dark' points, which are relatively easy to fit.

One complete fitted model as well as fit data and residuals is shown in Fig. 5 for one incidence angle. It can be seen that the largest residuals appear in the plane of incidence at polar angles slightly larger than the direction of the ideal specular reflection. Fig. 6 shows cross-sections of the of model and data in ϕ_{r}-direction. At small polar angles of reflection θ_{r}, the model fits quite well, whereas at $\theta_{\mathrm{r}} = 60^\circ$ a larger deviation occurs at the maximum.

As with the decrease of the appearent roughness, the occurrence of specular reflection for grazing incidence is

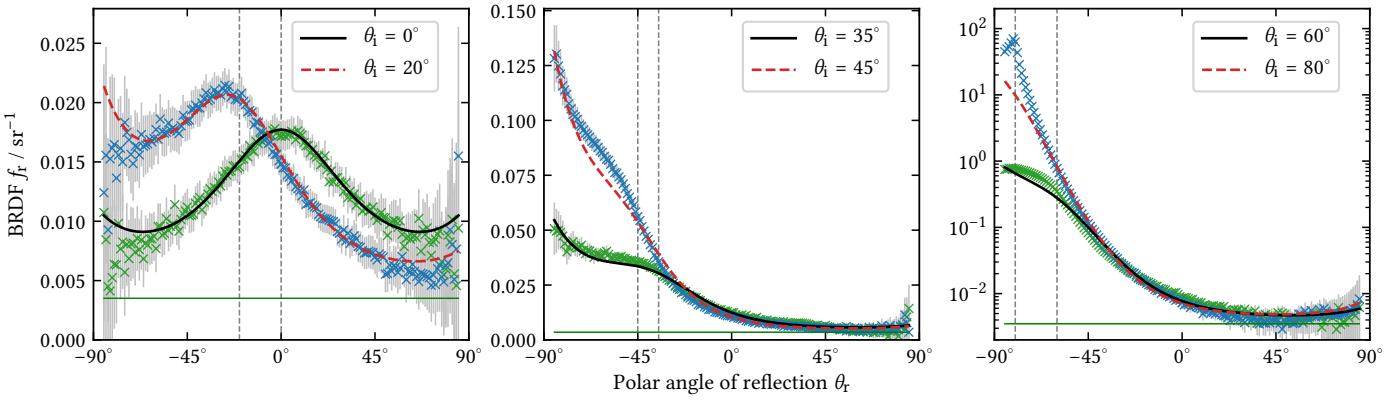

Figure 3: Measured BRDF of Pyromark in the plane of incidence (points) and fit with the Cook–Torrance model (lines) for several incidence angles θ_i. The fit is good for small incidence angles, but shows increasing deviation at larger angles (regression standard errors for the individual data sets are shown in Fig. 4). Separate roughness parameters α have been used for each of the 17 incidence angles, but the values for the index of refraction n and the uniform diffuse radiation $R_{\mathrm{dh,Lam}}$ (shown as horizontal green line) are the same for all incidence angles. The angles of ideal specular reflection are indicated.

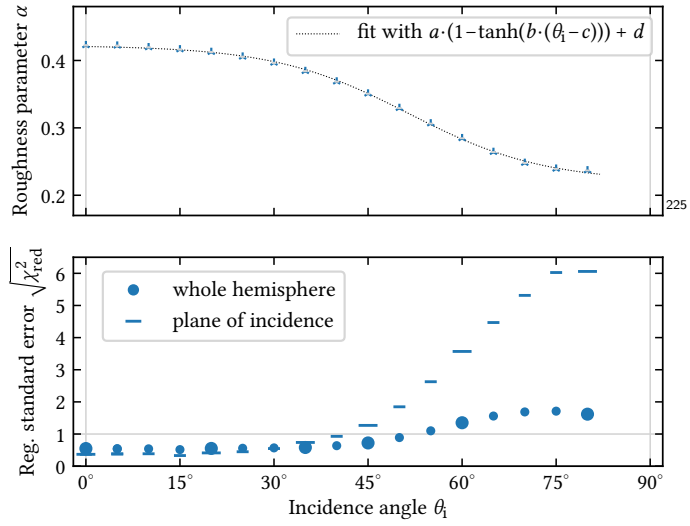

Figure 4: Roughness parameter α and regression standard error of the individual data sets for the fit with the Cook–Torrance model. Incidence angles shown in Fig. 3 are depicted with larger markers. The decrease of the roughness parameter has been captured with an empirical fit function.

not included in the CT model. This can clearly be seen in Fig. 3 for incidence angles of 60° and 80°. For those angles, the measured data around the direction of the specular reflection lies well above the values predicted by the model.

The lack of the ability to describe the appearance of specular reflection together with the need of the emprical function of Eq. 20 to describe the decline of the appearent surface roughnes make the CT model somewhat unsatisfactory. Therefore the more complex wave-optical model introduced by He et al. (1991) is investigated in the next section.

He–Torrance (HT) model

The He–Torrance model in the form it is applied here has five fit parameters: The index of refraction n, a vertical measure of roughness σ, a horizontal length measure τ, the uniform diffuse part $R_{\mathrm{dh,Lam}}$ and the half-width w of the specular cone of reflection. The incident radiation is assumed to be monochromatic with a wavelength of 585 nm. The simultaneous fit of the data for all incidence angles has a total standard error of 1.83 and yielded the follow-

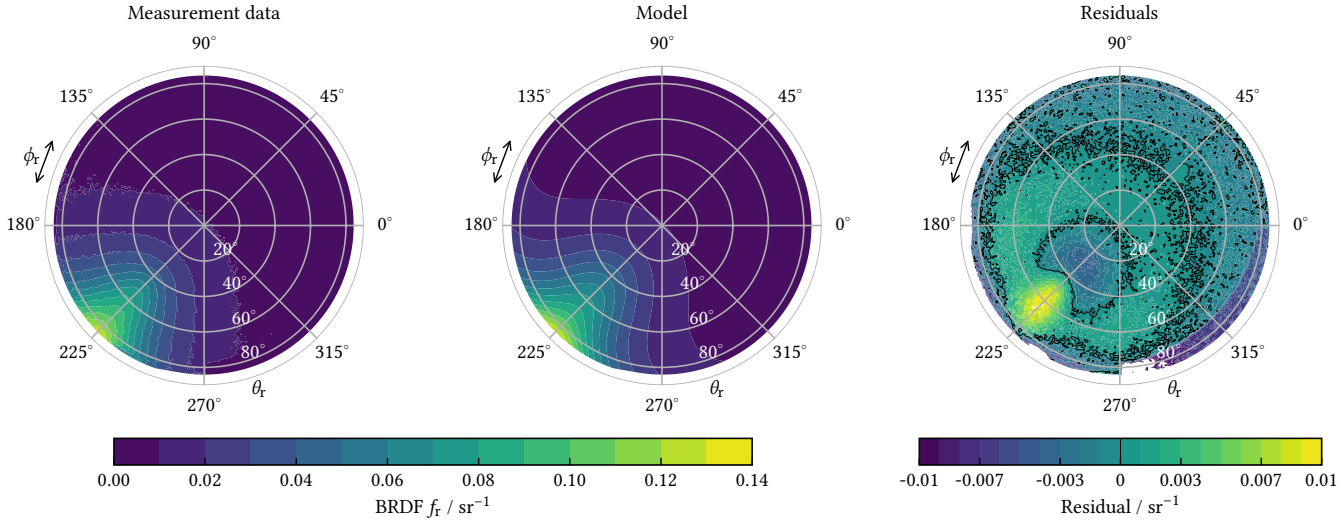

Figure 5: Measured BRDF of Pyromark in whole hemisphere, fit with the Cook–Torrance model and fit residuals. The data is the same as in Fig. 2: Incidence angles are $\theta_i = 45°$ and $\phi_i = 45°$. The model gives a good description of the angluar distribution of the reflected radiation. The largest residuals occur in the plane of incidence at polar angles θ_r between 45° and 75°.

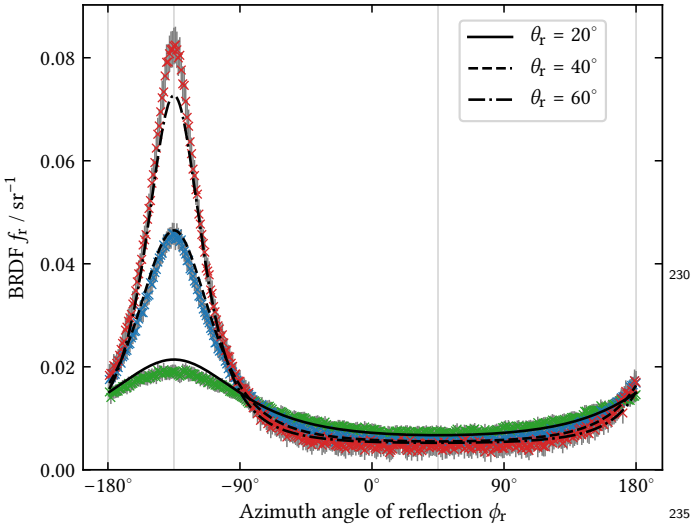

Figure 6: Cross-sections of the data in Fig. 5 in ϕ-direction, i.e. along the circle in Fig. 5 corresponding to the given value of θ_r: BRDF of Pyromark and fit with the Cook–Torrance model as a function of the azimuth angle of reflection for three different polar angles of reflection θ_r. The incidence angles are always $\theta_i = 45°$ and $\phi_i = 45°$.

ing parameters:

$$n_{HT} = 1.32$$
$$\sigma_{HT} = 0.281\,\mu m$$
$$\tau_{HT} = 1.635\,\mu m$$
$$R_{dh,Lam,HT} = 0.0169$$
$$w = 4.5°$$

Fit results in the plane of incidence for some incidence angles are shown in Fig. 7. Due to the fact that the HT model has fewer free parameters (5) than the fit with the CT model (19), the fit to the data is clearly less accurate. Above $\theta_r = 60°$, a specular part is emerging, but nevertheless the model values are considerably lower than the data. It can also be seen that the sharp edges of the unit function describing the specular component are not present in the data. The fit value for the half-width w of the specular cone is considerably higher than what would be expected from the divergence of a beam which is reflected from a specularly reflecting sample: The divergence of this beam is 1.4° in the photogoniometer. One reason for the widening of the beam of the specular reflection could be that the surface is in fact smooth at the wavelength scale as

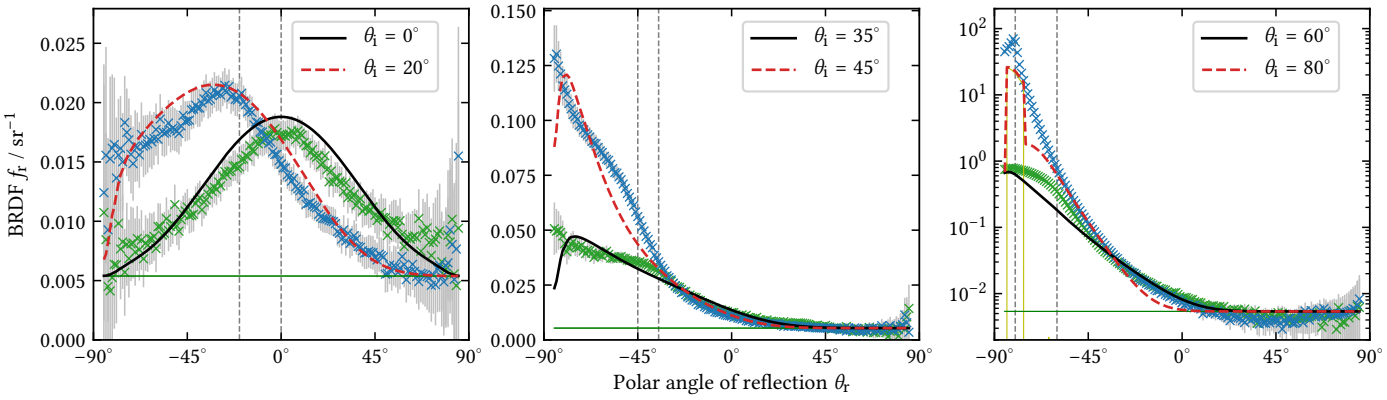

Figure 7: Measured BRDF of Pyromark in the plane of incidence (points) and fit with the He–Torrance model (lines) for several incidence angles θ_i. A common set of 5 physically meaningful fit parameters has been used to fit all incidence angles simultaneously, which makes the model less adaptable to the data than the Cook–Torrance model with 19 free fit parameters. The regression standard errors for the individual data sets are shown in Fig. 8. The uniform diffuse part of the model is shown as a horizontal green line, the specular share in yellow, which appears only at large θ_i.

well as at the (visible) macroscopic scale, but that there is an intermediate roughness in the order of several µm. Small undulations on the surface were observed under the microscope, which could be responsible for a broadening of the specular cone.

Standard regression errors for the individual hemispherical data sets as well as solely in the plane of incidence are shown in Fig. 8. All errors are langer than those obtained with the CT model, and particularly large errors occur in the plane of incidence.

Comparison of the two models

Two fit values of the two models, the index of refraction n and the uniform diffuse part $R_{\mathrm{dh,Lam}}$, can easily be compared, and there is no agreement between the models, at least not within the uncertainties provided by the numerical fit.

The comparison of the roughness parameter α of the CT model with the vertical measure of roughness σ and the horizontal length scale τ of the HT model is possible in an approximate manner: If the surface in the HT model is assumed to consist of regular undulations (Fig. 9) with height σ and distance τ, the term

$$\frac{2\sigma}{\tau} = m \qquad (21)$$

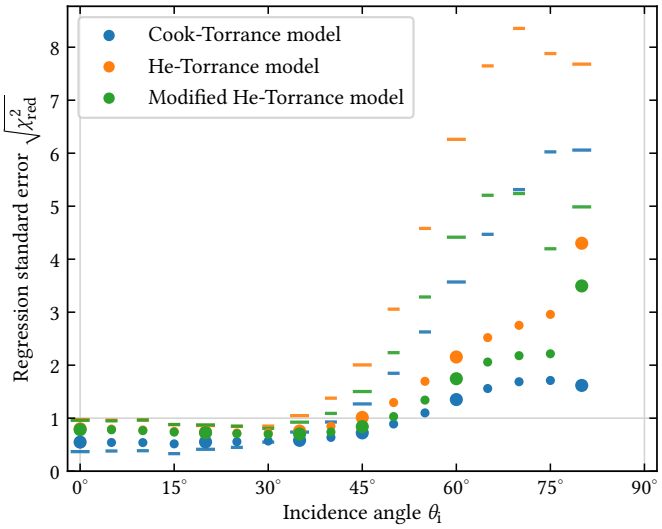

Figure 8: Regression standard errors for the different models in Fig. 3, Fig. 7 and Fig. 11. The errors have been evaluated hemispherically (points) as well as only in the plane of incidence (bars) to emphasize the lower fit quality around the direction of the specular highlight.

is an estimate of the mean absolute value of the slope of the surface m. This evaluates to

$$m_{\mathrm{HT}} = 0.34$$

with the obtained fit parameters.

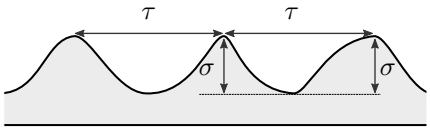

Figure 9: Schematic simplification of a rough surface with a horizontal and a vertical length measure. The parameters σ and τ are parameters of distributions which describe a class of statistical surfaces.

In the CT model, with the range of the roughness parameter given in Fig. 4, the mean slope is (Eq. 13)

$$0.38 < m_{\mathrm{CT}} < 0.66 \ .$$

In this interpretation, the slope which is seen by the HT model is almost the same as the mean slope obtained with the CT model, taking the limit of the sigmoidal function for α towards grazing incidence.

Directional hemispherical reflectance

Not only the BRDF of the models can be compared with the measured data, but also the directional hemispherical reflectance, which can be calculated from the models using Eq. 8. Fig. 10 shows the values obtained for the CT and the HT models and the modified HT model (see next paragraph). As the CT model relies on the empirical fit of the roughness parameter α, only a slight extrapolation beyond the domain of the fit is done. For large angles, the CT model predicts less reflection than actually observed. This might be due to the neglection of the specular reflection. The HT model has a similar fit quality for lower angles, but the reversal point at $\theta_{\mathrm{i}} = 82°$ seems completely implausible, as a monotonic increase of the reflectance towards grazing incidence is expected. We identified the factor $G_{\mathrm{HT1}}(\theta_{\mathrm{i}}, \sigma, \tau)$ of Eq. 18 to be the cause of this behaviour. If this factor is set to 1 for all incidence angles, the refectance does not show a reversal point anymore, but instead increases monotonically with increasing incidence angle θ_{i}. Setting this factor to 1 implies that there is not any shadowing of the specular part of the reflection, that depends on the incidence angle. Physically, this claim might be justifiable, as the specular reflection occurs on a smooth surface which may not be able to cause much shadowing, if any at all.

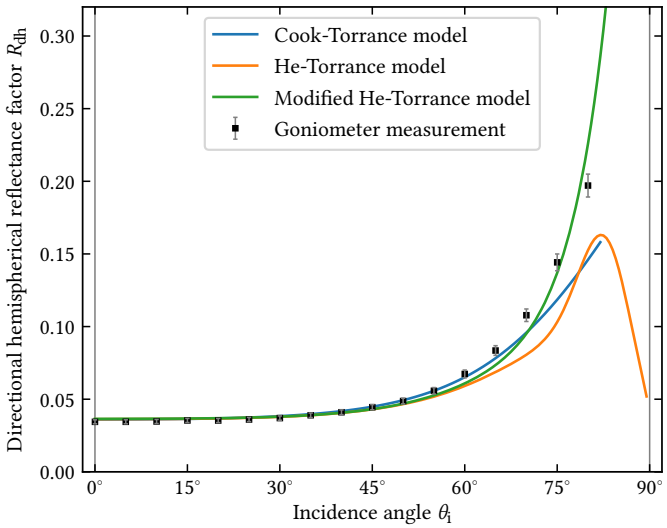

Figure 10: Dependence of the directional hemispherical reflectance factor R_{dh} on the incidence angle for the Pyromark sample and prediction of three different models. The α fit of the Cook–Torrance model is only used until 82°. The decrease of the reflectance in the unmodified standard He–Torrance model towards large angles is not plausible, therefore we propose a modification of the model with less shadowing.

Encouraged by this observation, we hence propose the following slight modifications to the HT model.

4. Modified He–Torrance model

4.1. Theory

We identified three possible modifications of the specular part of the He–Torrance model (Eq. 17) to improve the match with our data. First of all, we suggest replacing the specular unit cone Δ with a gaussian profile Γ, as we did not observe specular cones with sharp edges. As mentioned above, a gaussian profile in place of the unit cone

could be motivated by an unevenness of the surface. Potential structures with a horizontal extent of about 50 µm were observed under the microscope. A superposition of specular reflections from numerous undulations on the surface might in fact add up to a gaussian profile. We also found that the model quality is greatly improved if the gaussian profile is allowed to have different widths w_θ and w_ϕ in the θ and in ϕ directions, which adds one more fit parameter to the model:

$$\Gamma = \exp\left(\frac{-(\phi_\mathrm{r} - \phi_\mathrm{i} - \pi \mod 2\pi)^2}{(2w_\phi)^2}\right) \cdot \exp\left(\frac{-(\theta_\mathrm{r} - \theta_\mathrm{i})^2}{(2w_\theta)^2}\right) \tag{22}$$

Whereas the solid angle of the specular cone $\mathrm{d}\omega_\mathrm{i}$ in Eq. 17 is trivial to calculate in the case of the unit function, we propose the following solid angle for the gaussian profile, calculated analogously to $\mathrm{d}\omega_\mathrm{i}$ of the unit function:

$$\mathrm{d}\omega_\mathrm{i,g} = \int_0^{2\pi} \int_0^{\pi/2} \Gamma \sin(\theta_\mathrm{r}) \cdot \mathrm{d}\theta_\mathrm{r} \mathrm{d}\phi_\mathrm{r} \tag{23}$$

The second modification is the modification of the shadowing in the specular part that was described previously. Whereas setting the component $G_\mathrm{HT1}(\theta_\mathrm{i}, \sigma, \tau)$ that depends on incidence angle to 1 would suffice to eliminate the unphysical behaviour of the hemispherical reflectance factor R_dh, we obtained even better fit results by eliminating the shadowing in the specular part completely and setting G_HT to 1.

The third modification we make is to change θ_i in Eq. 17 to

$$\theta_\mathrm{m} = \arccos(\mathbf{r} \cdot \mathbf{i}) \,/\, 2 \ ,$$

which is the actual angle of incicence (and also reflection) on the microfacets. He et al. (1991) do not make it very clear whether θ_i or θ_r should be used in the denominator of Eq. 17, and indeed it does not make much difference for narrow cones of specular reflection.

With the three modifications, the modified specular part $f_\mathrm{r,sp,mod}$ has the following expression:

$$f_\mathrm{r,sp,mod} = \frac{F(\frac{\theta_\mathrm{i}-\theta_\mathrm{r}}{2}, n) \cdot \mathrm{e}^{-g}}{\cos\theta_\mathrm{m} \cdot \mathrm{d}\omega_\mathrm{i,g}} \cdot \Gamma \tag{24}$$

4.2. Fit results

Fit results of the modified HT model are shown in Fig. 11. Compared to the unmodified model, the decrease of the total regression standard error from 1.83 to 1.49 is not very large, and also the hemispherical values for the individual data sets (Fig. 8) do not improve much. But if the error is considered only in the plane of incidence, the improvement is clear: For large incidence angles θ_i, the modification reduces the errors by about one third.

The fit parameters after the modifications are

$$\begin{aligned} n_\mathrm{HTm} &= 1.34 \\ \sigma_\mathrm{HTm} &= 0.183\,\mu\mathrm{m} \\ \tau_\mathrm{HTm} &= 1.014\,\mu\mathrm{m} \\ R_\mathrm{dh,Lam,HTm} &= 0.0157 \\ w_\theta &= 14.9^\circ \\ w_\phi &= 3.2^\circ \ . \end{aligned}$$

The fit values for σ and τ differ greatly from the values obtained with the unmodified model, but their ratio is rather similar:

$$\frac{\sigma_\mathrm{HT}}{\tau_\mathrm{HT}} \approx 0.172 \qquad \frac{\sigma_\mathrm{HTm}}{\tau_\mathrm{HTm}} \approx 0.180$$

The values for R_dh which are obtained with the modified model are shown in Fig. 10. The difference to the standard model is small for small incidence angles, but there is a strong improvement for large angles.

5. Application of the models to solar-thermal central receivers

The basic motivation of this paper is to address high-temperature solar-thermal central receivers. However, all results were determined only at ambient temperature. The validity of transferring these results to the elevated operating conditions will be discussed briefly here. Moreover, while the experiments were conducted using white light and a photodiode with a V(λ) spectral response, the spectrally resolved behaviour of the BRDF is important information to understand the radiative performance and

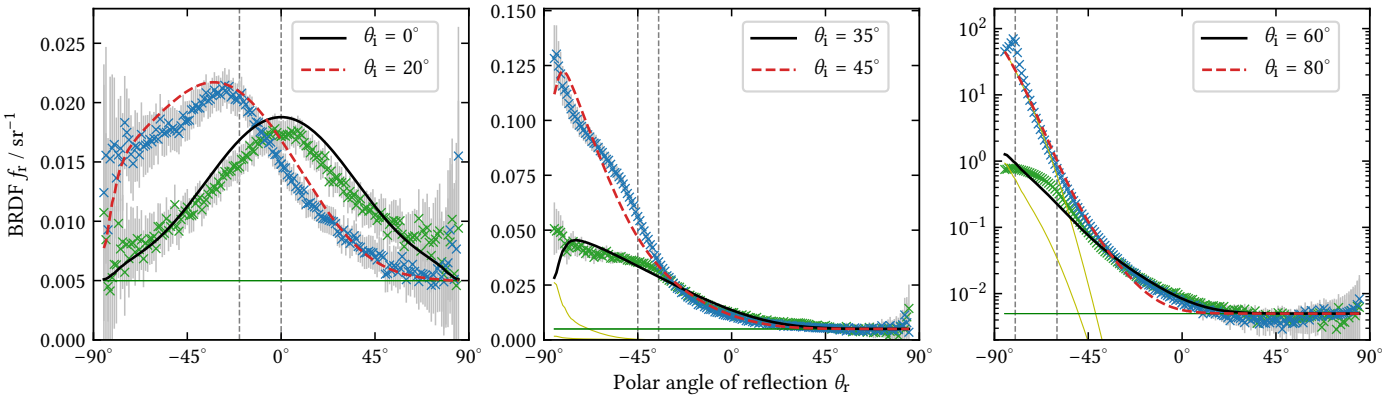

Figure 11: Measured BRDF of Pyromark in the plane of incidence (points) and fit with the modified He–Torrance model (lines) for several incidence angles θ_i. Compared to the original He–Torrance model, three modifications of the specular contribution have been made, resulting in one additional fit parameter. The regression standard errors for the individual data sets are shown in Fig. 8. The uniform diffuse part of the model is shown as green line, the appearing specular share in yellow.

losses from central receivers.[6] This section describes how the models used can be adapted to different thermal and spectral conditions.

5.1. Temperature dependence of the BRDF

We assume that the model parameters describing the roughness of the surface (α, σ and τ) do not change significantly with a varying surface temperature. Equally, we do not expect any temperature-dependent change in the parameter $R_{\mathrm{dh,Lam}}$, describing the diffuse scattering. The only temperature-dependent feature of the two used BRDF models could presumably be the index of refraction n. However, Ho et al. (2012) report that within the solar spectrum, the spectral directional absorptance of Pyromark does not vary significantly with temperature between 26 °C and 600 °C. Since the absorptance is determined by the refractive index of the material, this observation leads to the conclusion that there is no strong temperature dependence of the refractive index of Pyromark and therefore also no strong temperature dependence of the BRDF.

[6] The spectral range which is important to determine the thermal emissivity is centered around a wavelength in the MIR and would need separate experimental investigation.

5.2. Spectral dependence of the BRDF

In this study, all BRDF measurements were conducted using white light with a spectral composition comparable to sunlight. The wavelength dependence of the BRDF was not investigated. The same measurements are also feasible for different wavelength ranges, which will be the subject of future research. However, even without available experimental data, predictions regarding the wavelength dependence of the BRDF can be drawn from the theoretical models.

Just as with the temperature dependence, in both models a possible spectral dependence of the refractive index n may be taken into account. However, — analogously to the argumentation above — there is experimental evidence that the spectral directional absorptance of Pyromark does not vary greatly within the solar spectrum (Ho et al., 2012). Therefore the variation of the index of refraction and the resultant change of the BRDF will be low.

In contrast to the geometrical Cook–Torrance model, the He–Torrance model explicitly contains the wavelength of the incident light as a model parameter. Within the solar spectral range, a modification of this parameter changes the value of the BRDF only slightly. That the BRDF of Pyromark is essentially independent of wavelength (within the solar spectral range) is also indicated by the fact that

only the ratio of the two roughness parameters σ and τ can be precisely determined in the fits, and not their exact value. This implies that there is only a weak wavelength dependence due to geometrical effects.

The considerations in this section suggest that it would be interesting to precisely measure the temperature and wavelength dependence of the refractive index of Pyromark in order to quantify the effect on the variation of the BRDF, but that the effect can be expected to be small.

The conducted work focuses on the description of measurement data with suitable models. While the exact BRDF values and the angular dependence are expected to differ slightly according to the wavelength of the radiation or the material temperature, a stronger influence of the application technique or of degradation is expected. The presented models, however, provide a very good estimate of the full BRDF based only on a few measurements, which is useful e.g. for design simulations and performance prediction during plant operation.

6. Conclusion

In this article, we investigate the predictions of the BRDF of solar thermal receiver coatings by use of three physical models. The investigated models perform differently: The Cook–Torrance model provides the best overall fit, but it is partly empirical and lacks an explicit specular component. The standard He–Torrance model shows inferior fit quality and it is implausible concerning the integrated reflectance, but all of its model parameters are physically meaningful. The modified He–Torrance model also performs worse than the Cook–Torrance model considering the hemispherical regression error, but in the plane of incidence for large incidence angles, the performance is similar to the Cook–Torrance model.

In total, all examined models allow a good qualitative description of the amplitude of the reflected radiation, depending on the polar incidence angle and the polar and azimuthal angles of reflection. This is particularly noteworthy, as the amplitude of the BRDF ranges over more than three orders of magnitude, whereas none of the models actually contains a parameter — apart from the small uniform diffuse share — which is directly fit to the amplitude of the radiation.

The fact that all parameters of the He–Torrance model have a clear physical meaning makes it possible to trace the distribution of the reflected radiation back to material and surface parameters, which enables systematic modifications of the radiative characteristic by modifying surface properties. The separation of the reflected radiation into different components of uniformly diffuse, directionally diffuse and specular reflection also allows a deeper understanding of the processes involved in the process of reflection.

If a very exact description of the BRDF is desired, which particularly captures the behaviour around the direction of the specular reflection, the tested models appear not to be sufficiently accurate. However, they can be very useful if only a limited data set of measured BRDF values of a material is available. Since detailed measurements of the BRDF involve complex setups and take hours to several days, this may frequently be the case. With one of the presented models, it would be possible to conduct a fast BRDF measurement e.g. only in the plane of incidence and apply a model fit to extrapolate to the whole hemisphere.

Applications of the BRDF model of absorber paints to effects in CRS receivers and solar tower plants are subject to ongoing and future research.

Acknowledgements

The authors would like to thank Peter Apian-Bennewitz for helpful discussions and valuable suggestions, Johannes Hanek for constant support with the measurements in the

goniometer and Sophie Gledhill for her invaluable aid in the sample preparation.

The presented work was funded by the German Federal Ministry for Economic Affairs and Energy (code 0324175). The authors of this publication are responsible for its contents.

References

Ambrosini, A., Boubault, A., Ho, C.K., Banh, L., Lewis, J.R., 2019. Influence of application parameters on stability of Pyromark® 2500 receiver coatings, in: Proceedings of the 24th SolarPACES International Conference (SolarPACES 2018). doi:10.1063/1.5117514. 030002.

Apian-Bennewitz, P., 2010. New scanning gonio-photometer for extended BRTF measurements, in: Reflection, Scattering, and Diffraction from Surfaces II, SPIE. pp. 185 – 204. doi:10.1117/12.860889.

ASTM, 2005. E2387-05: Standard Practice for Goniometric Optical Scatter Measurements. ASTM International. West Conshohocken, PA. doi:10.1520/E2387-05.

Bauer, R., 2000. Distribution of Points on a Sphere with Application to Star Catalogs. Journal of Guidance, Control, and Dynamics 21, 130–137. doi:10.2514/2.4497.

Beckmann, P., Spizzichino, A., 1963. The scattering of electromagnetic waves from rough surfaces. 4 ed., Pergamonn Press, London.

Bern, G., Schöttl, P., van Rooyen, D.W., Heimsath, A., Nitz, P., 2019. Parallel in-situ measurement of heliostat aim points in central receiver systems by image processing methods. Solar Energy 180, 648–663. doi:10.1016/j.solener.2019.01.051.

Bitterling, M., Bern, G., Schöttl, P., Gledhill, S., Wilson, H.R., Heimsath, A., Nitz, P., 2020. Measuring and Modelling the BRDF of Solar Receiver Paints, in: Proceedings of the 25th SolarPACES International Conference, 1-4 October 2019, Daegu, South Korea. In review.

Cook, R., Torrance, K.E., 1982. A Reflectance Model for Computer Graphics. ACM Transactions on Graphics 1, 7–24. doi:10.1145/800224.806819.

Coventry, J., Burge, P., 2017. Optical properties of Pyromark 2500 coatings of variable thicknesses on a range of materials for concentrating solar thermal applications, in: Proceedings of the 22nd SolarPACES International Conference (SolarPACES 2016). doi:10.1063/1.4984355. 030012.

He, X.D., Torrance, K.E., Sillion, F.X., Greenberg, D.P., 1991. A Comprehensive Physical Model for Light Reflection. Computer Graphics 25, 175–186. doi:10.1145/127719.122738.

Ho, C.K., Mahoney, A.R., Ambrosini, A., Bencomo, M., Hall, A., Lambert, T.N., 2012. Characterization of Pyromark 2500 Paint for High-Temperature Solar Receivers, in: Proc. of ASME 2012 6th International Conference on Energy Sustainability & 10th Fuel Cell Science. doi:10.1115/ES2012-91374.

Li, H., Torrance, K.E., 2005a. An Experimental Study of the Correlation between Surface Roughness and Light Scattering for Rough Metallic Surfaces, in: Proc. of SPIE, p. 58780V. doi:10.1117/12.617637.

Li, H., Torrance, K.E., 2005b. Background Data for Validation of the He-Torrance Model. Technical Report PCG-05-02. Program of Computer Graphics, Cornell University. Ithaca, NY.

Modest, M., 2003. Radiative Heat Transfer. 2 ed., Academic Press.

Nicodemus, F.E., Richmond, J.C., Hsia, J.J., Ginsberg, I.W., Limperis, T., 1977. Geometrical Considerations and Nomenclature for Reflectance. National Bureau of Standards. Washington, D.C.

Offergeld, M., Röger, M., Stadler, H., Gorzalka, P., Hoffschmidt, B., 2019. Flux Density Measurement for Industrial-Scale Solar Power Towers Using the Reflection off the Absorber, in: Proceedings of the 24th SolarPACES International Conference (SolarPACES 2018). doi:10.1063/1.5117617. 110002.

Röger, M., Herrmann, P., Ulmer, S., Ebert, M., Prahl, C., Göhring, F., 2014. Techniques to Measure Solar Flux Density Distribution on Large-Scale Receivers. Journal of Solar Energy Engineering 136, 031013. doi:10.1115/1.4027261.

Rubin, E.B., Shin, S., Chen, Y., Chen, R., 2019. High-temperature stable refractory nanoneedles with over 99% solar absorptance. APL Materials 7, 031101. doi:10.1063/1.5084086.

Siegel, R., Howell, J.R., 1992. Thermal Radiation Heat Transfer. 3 ed., Hemisphere Publishing Corporation, Washington.

Smith, B.G., 1967. Geometrical Shadowing of a Random Rough Surface. IEEE Trans. on Antennas and Propagation AP-15, 668–671. doi:10.1109/TAP.1967.1138991.

Stover, J.C., 1995. Optical Scattering: Measurement and Analysis. 2 ed., SPIE Press, Bellingham, WA.

Torrance, K.E., Sparrow, E.M., 1967. Theory for Off-Specular Reflection From Roughened Surfaces. Journal of the Optical Society of America 57, 1105–1114. doi:10.1364/JOSA.57.001105.

Trowbridge, T.S., Reitz, K.P., 1975. Average irregularity representation of a rough surface for ray reflection. Journal of the Optical Society of America 65, 531–536. doi:10.1364/JOSA.65.000531.

Tsuda, K., Murakami, Y., Torres, J.F., Coventry, J., 2018. Development of high absorption, high durability coatings for solar receivers in CSP plants, in: Proceedings of the 23rd SolarPACES International Conference (SolarPACES 2017). doi:10.1063/1.5067075. 040039.

Walter, B., Marschner, S., Li, H., Torrance, K., 2007. Micro-

facet Models for Refraction through Rough Surfaces, in: Proc. of EGSR, pp. 195–206. doi:10.2312/EGWR/EGSR07/195-206.